Comparative Evaluation of Radio Propagation Properties at 15 GHz and 60 GHz Frequencies

Dmitrii Solomitckii, Vasilii Semkin, Reza Naderpour, Aleksandr Ometov, and Sergey Andreev

***Abstract*—Due to explosive growth in the mobile data demand, millimeter-wave (mmWave) spectrum is to become one of the key enablers for the next-generation 5G wireless. Accurate characterization of mmWave channels has crucial implications on 5G network planning – as compared to more conventional frequency bands – due to a higher impact that surrounding objects have on the radio propagation. In this work, we contribute mmWave channel measurements and compare our obtained results across several metrics of interests, mindful of previously standardized models. The proposed analysis is conducted for a typical mmWave system deployment operating at 15 and 60 GHz. The evaluation studies a difference between the obtained results for the two frequency bands considered, as well as verifies their predictability when utilizing modern modeling considerations.**

***Index Terms*—mmWave systems, radio propagation, urban deployments, practical measurements, channel sounding**

I. Introduction

In recent years, the number of mobile devices and multimedia applications has been increasing tremendously [1]. Such an explosive growth brought additional pressure to develop new solutions that would support the continuously accelerating traffic demand over a limited spectrum [3]. Cellular operators already face overloads on their existing networks. An intuitive step towards the paradigm of millimeter-wave (mmWave) band utilization as the novel frontier for the next-generation wireless networks, named 5G, is expected to be made soon [5].

Commonly, mmWave spectrum is defined to reside from 3 to 300 GHz [6]. It will support relatively wide bands of up to 2 GHz [7]. In practice, the mmWave system performance may enable multi-gigabit throughputs for bandwidth-hungry multimedia services, such as demanding cellular communications [8], live indoor data streaming [10], high definition (HDV) and ultra-high definition video (UHDV) [11], and many others.

Despite the benefits, mmWave propagation opens new challenges for the researchers and vendors [12]. Those are, for example, (i) higher propagation losses, (ii) noticeable level of diffuse scattering from small objects, (iii) utilization of multi-antenna systems with narrower beams, and (iv) higher probability of blockage. All of these challenges make accurate channel parametrization more crucial to facilitate planning and deployment of the 5G mmWave cellular networks.

Extensive measurements of outdoor mmWave bands (at 28, 38, and 73 GHz) have already been completed in [13]–[15], where large-scale channel properties were investigated. For instance, it was demonstrated that mmWave links are suitable for both line-of-sight (LoS) and non-line-of-sight (NLoS) conditions in the range of up to 200 m. Another wide-band channel sounding campaign has been performed at 59-66 GHz for a single polarization case in [16], [17] and at 70 GHz for dual-polarization in [18].

These results confirm the advantage of the polarization diversity even in relatively simple scenarios. Measurements of the single-input single-output (SISO) wide-band channel at 28 GHz have been presented in [19]. Here, the methods of synthesizing and aligning were discussed by contributing advanced measurements of spatial and temporal channel characteristics. Another study on SISO sounding in an urban deployment [20] demonstrated the consideration of 10 GHz and 60.4 GHz frequencies.

This work contributes propagation measurements at 15 and 60 GHz around buildings in Helsinki area (Aalto University campus). The present studies extend the previous research [21] in terms of ray-tracing accuracy considerations. We remind that 60 GHz frequency is already in use by the indoor IEEE 802.11ad technology. It is also considered as the candidate carrier for IEEE 802.11ay. The second frequency appears to be of interest within the academic community, as e.g., in [22], [23], and may be of value in the deployment of prospective 5G systems.

The rest of the paper is organized as follows. Our sounding equipment and the scenario of interest are described in Section II. Further, the obtained results and the corresponding analysis are offered in Section III. The last section concludes the work.

II. Scenario of Interest

In this work, we consider a three-floor building with a flat roof covered by a roofing felt. The measurements were conducted at the Aalto University campus in Espoo, Finland. The deployment under study is illustrated in Fig. 1.

According to the construction plan, the types of the building materials are as follows: brick, foliage, metal, and plastic. The receiver was fixed in its position, while the transmitter was moved around according to 6 locations shown in Fig. 1. The link distances during the measurements were 53, 57, 60, 63, 89, and 118 meters, respectively. All of the links are LoS, but foliage and diffuse scattering sources may intersect the Fresnel zone between the antennas. As a result, together

Correspondence e-mail: dmitrii.solomitckii@tut.fi

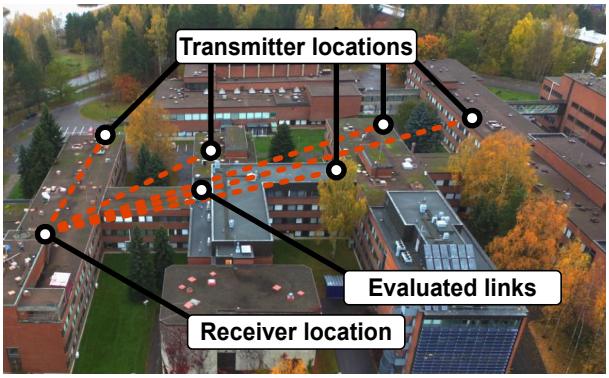

Fig. 1: Photo of a real-life mmWave deployment.

with the dominant LoS paths, additional scattered multi-path components might be observed as well.

In order to acquire complete radio channel information, co- and cross-polarization measurements have been carried out. The sounding setup for both devices is summarized in Fig. 2. The position of the receiving antenna was fixed and it was rotated in the azimuth plane over $360°$ with a $5°$ step. We utilized the diamond antenna measurement system, where the main parameters are listed in Table I.

TABLE I: Main parameters of the measurement system.

Parameter	60 GHz	15 GHz
IF signal	$1-5$ GHz	n/a
LO signal	14.5 GHz	n/a
RF signal	$59-63$ GHz	$14-15$ GHz
Center frequency	61 GHz	14.2 GHz
LO power	24.5 dBm	n/a
VNA power	-15 dBm	-15 dBm
No. of sweep points	10001 pcs.	10001 pcs.
TX antenna	Bicone, 2 dBi	Bicone, 2 dBi
RX antenna	Horn, 19 dB	Horn, 19 dBi
HPBW of the RX	$\phi = 10°$, $\theta = 40°$	$\phi = 10°$, $\theta = 40°$
Antenna interface	waveguide	SMA
Back-to-back calibration	20 dB attenuator	30 dB attenuator

A horn antenna with the gain of 19 dBi is utilized at the receiver side and a bicone antenna with the 2 dBi gain is deployed at the transmitter side. Optical fiber connects the devices to increase the accuracy of measurements. The channel sounding equipment is based on a vector network analyzer (VNA) that allows to measure phase-synchronized scattering parameters. A back-to-back calibration was performed before the actual measurements to reduce the equipment side effects.

Up- and down-converters are utilized to receive the signal in $59-63$ GHz frequency range. The intermediate frequency (IF) signal from the VNA and the local oscillator (LO) is converted to the optical signal and sent through the optical transmitter for each direction of the receiving antenna. At the receiver side, the signal is converted from optical to electrical and further transferred to the transmitter's mixer. Next, the LO

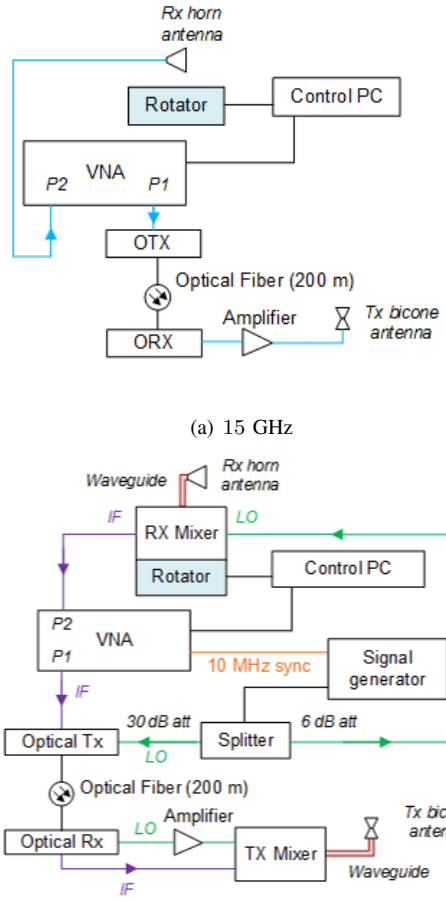

(a) 15 GHz

(b) 60 GHz

Fig. 2: Wide-band sounding equipment setup.

signal is amplified, while the IF signal is forwarded directly to the mixer. The LO and IF signals are up-converted to recover the RF signal.

The radio signal is firstly transmitted and then received by the receiver's horn antenna. It is then down-converted and the IF component is distinguished by using the LO signal from the signal generator. The 15 GHz channel sounder does not utilize up- and down-converters in contrast to the 60 GHz setup. The RF signal is generated by the VNA and further transmitted via the optical fiber to the optical receiver. Finally, the signal is amplified and sent to the transmitter's bicone antenna.

III. Obtained Results

In this section, we elaborate on the obtained channel propagation measurements and further compare them with the standardized models, such as those considered by 3GPP.

A. Measurements

First, we measure the complex channel impulse response (CIR) as a function of time delay and rotation angle $h(\theta, \tau)$. Further, co-polarized and cross-polarized power angular delay profile (PADP) is calculated as an absolute squared

CIR. An example of the PADP is shown in Fig. 3. Here, blue color represents the noise level and close to red color indicates the locations of the significant multi-path components in angular and time domains.

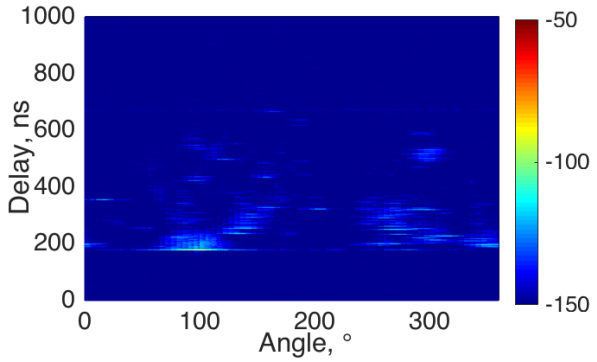

Fig. 3: Example of PADP for fixed transmitter position.

In order to evaluate the average degree of signal dispersion for a particular deployment, the power delay profile (PDP) is also obtained (see Fig. 4) as the spatial averaging of CIR

$$PDP(\tau) = \frac{1}{N}\sum_{n=1}^{N}|h(\theta,\tau)|^2, \tag{1}$$

where N is equal to 72 (360° divided by the 5° rotation step).

Further, the representations of co-polarized PDP and cross-polarized PDP are demonstrated in red and blue, correspondingly, in Fig. 4. The cross-polarized channel is evaluated via a 90° rotation of the receiving antenna.

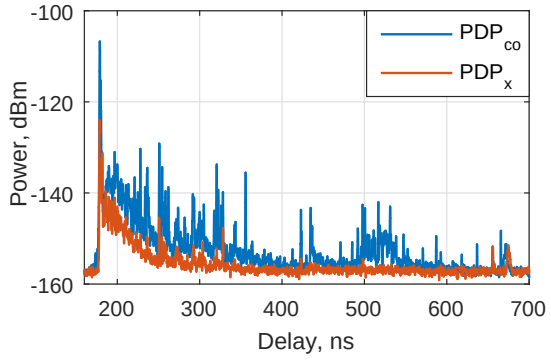

Fig. 4: Example of cross-polarized (red) and co-polarized (blue) measured PDPs.

B. Path Loss Analysis

The path loss (PL) is a major propagation property, which determines the quality of service (QoS) and reliability of a wireless link. The PL may predict the magnitude of the total received power for specific antenna positions. It is also highly sensitive to the presence of obstacles between the transmitter and the receiver. We further estimate the PL from the measured PDP and transmit power as follows

$$PL = P_{tx} - \int_{\tau_0}^{\tau_{exc.}} PDP d\tau, \tag{2}$$

where P_{tx} is the transmit power. The corresponding results are presented in Fig. 5. The empirical models (e.g., Friis and 3GPP model) shown in the figure also support the obtained results. Fading caused by the multipath propagation may alter the mean value of the PL by $3-5$ dB [24]. This is due to the multi-path components that constructively or destructively influence their sum at the receiver side with different phases and amplitudes defined by the propagation physics and the surrounding environment. Hence, the PL at 60 GHz is about $10-13$ dB higher as compared to the 15 GHz link.

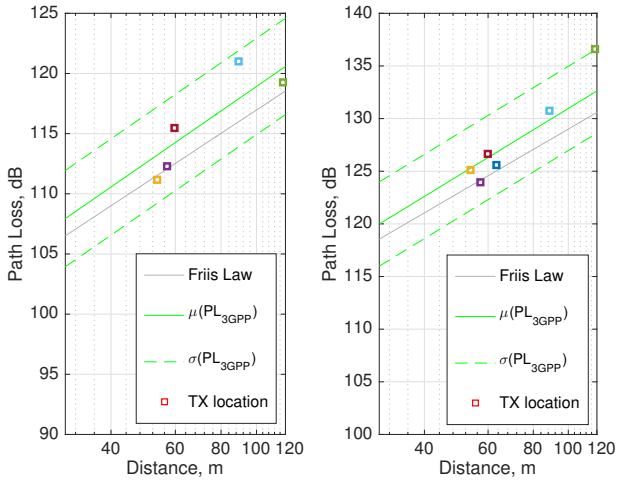

Fig. 5: Calculated PL for different transmitter locations at 15 GHz (left) and 60 GHz (right).

C. Delay and Angular Spread

The multi-path components arriving at the receiver are dispersed in angular and time domains due to the interaction with various obstacles. Such a behavior plays a dominant role in mmWave propagation, since the contribution by smaller objects is significantly higher as compared to that at lower frequencies. For example, the relative performance of the multi-antenna diversity and beamforming code books are highly dependent on the angular spread. Another important reason to consider the angular spread (AS) is related to inter-symbol interference (ISI) problem. Below, we estimate both the AS and the delay spread (DS) as a second moment statistics through root mean square (RMS) [25] as follows

$$\sigma_\tau = \sqrt{\frac{\int PDP(\tau)\tau^2 d\tau}{\int PDP(\tau)d\tau} - \bar{\tau}}, \tag{3}$$

and

$$\sigma_\theta = \sqrt{\frac{\int |exp(j\phi) - \mu_\phi|^2 PAS(\phi)d\phi}{\int PAS(\phi)d\phi}}, \tag{4}$$

where PDP is the power delay profile and PAS is the power angular spectrum, which characterizes the distribution of incoming power in the angular range. The corresponding results are presented in Table II.

TABLE II: Delay and angular spread for 15 GHz and 60 GHz

	60 GHz		15 GHz	
TX-RX Distance, m	**DS**	**AS**	**DS**	**AS**
53	19.7	16.1	17.7	18.7
57	22.2	15.2	24.2	16.8
60	16.3	13.2	14.7	10.7
63	15.2	11.0	16.7	10.0
89	14.0	9.9	12.7	11.1
118	12.4	4.0	n/a	n/a

Based on the obtained results, we can conclude that delay and angular spreads are almost identical for 15 and 60 GHz. Moreover, those are dependent on the distance: shorter distances significantly decrease the resulting values. From the physical perspective, higher distances lead to stronger attenuation of the multi-path components, thus angular and time dispersion decreases. We note that it also depends on the distribution, as well as on the type of the surrounding objects. For example, we observe that link 2 has more significant angular and delay spreads due to a higher density of objects distributed in the LoS between the transmitter and the receiver.

D. Cross-Polarization Ratio

The signal may suffer from intermediate bouncing from the surrounding obstacles during its propagation. Such interactions may affect the polarization, which in turn may cause significant losses at the receiver side. Following the electromagnetic theory, orthogonal orientation of two polarization vectors at the transmitter and receiver sides makes the losses significantly higher. The main sources of the polarization losses are reflection and diffuse scattering, while the contribution of diffraction is less significant. There are two main indicators that characterize this phenomenon: cross-polarization ratio (XPR) and cross-polarization discrimination (XPD) [26]. Based on the assumption that our channel is reciprocal, XPR can be selected as the metric of interest and calculated as follows

$$XPR = 10log_{10}(\frac{P_{co}}{P_x}), \tag{5}$$

where P_{co} and P_x are the co-polarized and cross-polarized values of power at the receiver, respectively. The cross-polarized component is collected by rotating the receiver antenna by 90°. The XPR is calculated as follows. First, we determine both co-polarized and cross-polarized PDP peaks of higher than noise floor by at least 10 dB. Then, this list is filtered and the XPR value is calculated, while the results are shown in Fig. 6.

Current wireless standards, such as 3GPP, propose a model for XPR predication as a log-normal distribution that is independent from both frequency and distance. However, it can be concluded from our measurement campaign that XPR is slightly dependent on the distance. This observation can be verified based on Fig. 6. Here, XPR decreases exponentially with the increasing distance between antennas, while its range of 5-13 dB is aligned with 3GPP reference values in [24].

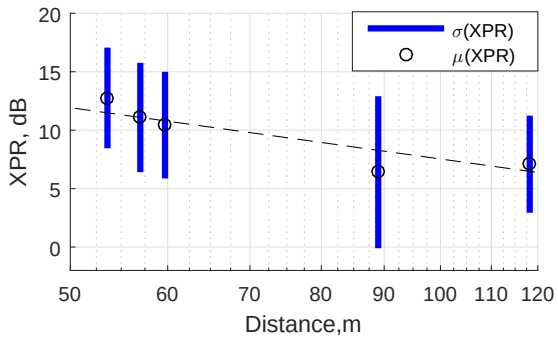

(a) 15 GHz

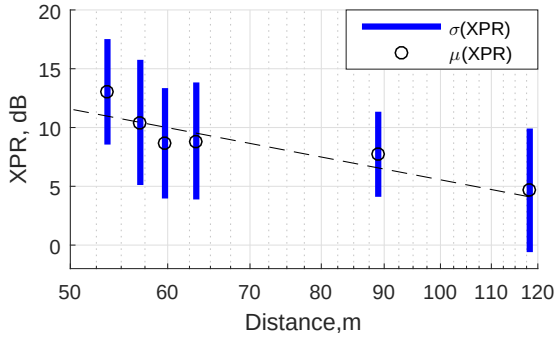

(b) 60 GHz

Fig. 6: XPR as a function of distance. Standard deviation (σ) is marked in blue.

Additional investigation has been conducted to determine how XPR depends on the orientation of the receiver antenna and the respective results are given in Fig. 7. Our produced output data demonstrates that XPR has its higher value in the LoS conditions by varying from 20 to 30 dB for all cases considered. However, the mean value is about 8 dB for both studied frequencies.

IV. Conclusion

This paper presented outdoor measurements of basic multi-path channel properties (path loss, delay and angular spread, as well as cross-polarization ratio) of a mmWave system deployed in the city of Helsinki. The measurement procedure was executed for 6 different links and the data has been validated against standardized models. Our final results demonstrated the similarities in most of the metrics of interest for both 15 and 60 GHz frequencies, except for the path loss, which is apparently higher at 60 GHz.

Acknowledgment

The publication was prepared with the support of the "RUDN University Program 5-100".

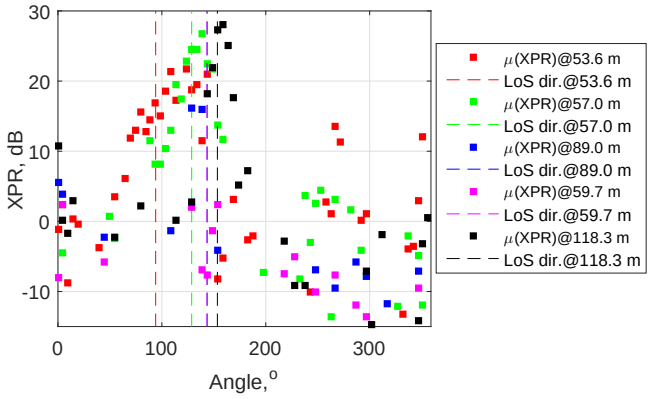

(a) 15 GHz

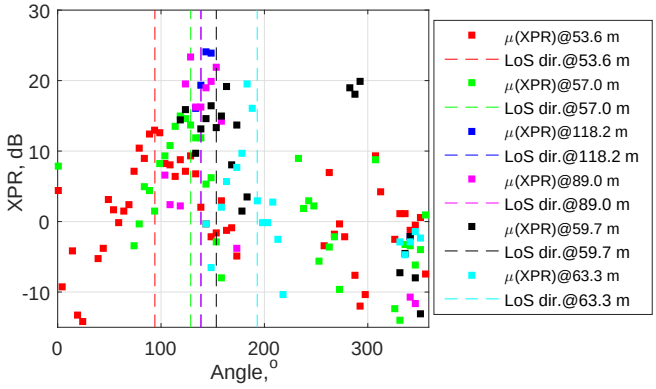

(b) 60 GHz

Fig. 7: XPR is demonstrating highest value when there is LoS.

REFERENCES

[1] Cisco, "Global mobile data traffic forecast 2016–2021." White Paper, 2017.

[2] A. Ponomarenko-Timofeev, A. Pyattaev, S. Andreev, Y. Koucheryavy, M. Mueck, and I. Karls, "Highly dynamic spectrum management within licensed shared access regulatory framework," *IEEE Communications Magazine*, vol. 54, no. 3, pp. 100–109, 2016.

[3] X. Gao, L. Dai, S. Han, I. Chih-Lin, and R. W. Heath, "Energy-efficient hybrid analog and digital precoding for mmWave MIMO systems with large antenna arrays," *IEEE Journal on Selected Areas in Communications*, vol. 34, no. 4, pp. 998–1009, 2016.

[4] S. Andreev, P. Gonchukov, N. Himayat, Y. Koucheryavy, and A. Turlikov, "Energy efficient communications for future broadband cellular networks," *Computer Communications*, vol. 35, no. 14, pp. 1662–1671, 2012.

[5] F. Boccardi, H. Shokri-Ghadikolaei, G. Fodor, E. Erkip, C. Fischione, M. Kountouris, P. Popovski, and M. Zorzi, "Spectrum pooling in mmWave networks: Opportunities, challenges, and enablers," *IEEE Communications Magazine*, vol. 54, no. 11, pp. 33–39, 2016.

[6] F. Khan and Z. Pi, "mmWave mobile broadband (MMB): Unleashing the 3–300GHz spectrum," in *Proc. of 34th Sarnoff Symposium*, pp. 1–6, IEEE, 2011.

[7] M. Ghosh, S. Salous, and Y. Gao, "Analysis of Wide-Band MIMO Measurements for the 60 GHz Band," in *Proc. of Wireless Communications and Networking Conference Workshops (WCNCW)*, pp. 1–6, IEEE, 2017.

[8] T. Bai and R. W. Heath, "Analysis of self-body blocking effects in millimeter wave cellular networks," in *Proc. of 48th Asilomar Conference on Signals, Systems and Computers*, pp. 1921–1925, IEEE, 2014.

[9] A. Samuylov, M. Gapeyenko, D. Moltchanov, M. Gerasimenko, S. Singh, N. Himayat, S. Andreev, and Y. Koucheryavy, "Characterizing spatial correlation of blockage statistics in urban mmWave systems," in *Globecom Workshops (GC Wkshps)*, pp. 1–7, IEEE, 2016.

[10] S. Deng, M. K. Samimi, and T. S. Rappaport, "28 GHz and 73 GHz millimeter-wave indoor propagation measurements and path loss models," in *Proc. of International Conference on Communication Workshop (ICCW)*, pp. 1244–1250, IEEE, 2015.

[11] D. Wu, J. Wang, Y. Cai, and M. Guizani, "Millimeter-wave multimedia communications: challenges, methodology, and applications," *IEEE communications Magazine*, vol. 53, no. 1, pp. 232–238, 2015.

[12] K. Huang and X. Zhou, "Cutting the last wires for mobile communications by microwave power transfer," *IEEE Communications Magazine*, vol. 53, no. 6, pp. 86–93, 2015.

[13] T. S. Rappaport, "Millimeter wave mobile communications for 5G cellular: It will work!," *IEEE Access, vol. 1, pp. 335-349, May 2013.*, 2013.

[14] T. S. Rappaport, F. Gutierrez, E. Ben-Dor, J. N. Murdock, Y. Qiao, and J. I. Tamir, "Broadband millimeter-wave propagation measurements and models using adaptive-beam antennas for outdoor urban cellular communications," *IEEE Transactions on Antennas and Propogation*, vol. 61, no. 4, pp. 1850–1859, 2013.

[15] S. Rangan, T. S. Rappaport, and E. Erkip, "Millimeter-wave cellular wireless networks: Potentials and challenges," *Proc. of the IEEE*, vol. 102, no. 3, pp. 366–385, 2014.

[16] A. P. G. Ariza, W. Kotterman, R. Zetik, M. Kmec, U. Trautwein, R. Muller, F. Wollenschlager, and R. S. Thoma, "60 GHz-ultrawideband real-time multi-antenna channel sounding for multi giga-bit/s access," in *Proc. of 72nd Vehicular Technology Conference Fall (VTC 2010-Fall)*, pp. 1–6, IEEE, 2010.

[17] A. P. G. Ariza, R. Müller, F. Wollenschläger, A. Schulz, M. Elkhouly, Y. Sun, S. Glisic, U. Trautwein, R. Stephan, J. Müller, *et al.*, "60 GHz ultrawideband polarimetric MIMO sensing for wireless multi-gigabit and radar," *IEEE Transactions on Antennas and Propagation*, vol. 61, no. 4, pp. 1631–1641, 2013.

[18] R. Müller, R. Herrmann, D. A. Dupleich, C. Schneider, and R. S. Thomä, "Ultrawideband multichannel sounding for mm-wave," in *Proc. of 8th European Conference on Antennas and Propagation (EuCAP)*, pp. 817–821, IEEE, 2014.

[19] S. Hur, Y.-J. Cho, J. Lee, N.-G. Kang, J. Park, and H. Benn, "Synchronous channel sounder using horn antenna and indoor measurements on 28 GHz," in *Proc. of International Black Sea Conference on Communications and Networking (BlackSeaCom)*, pp. 83–87, IEEE, 2014.

[20] R. J. Weiler, M. Peter, T. Kühne, M. Wisotzki, and W. Keusgen, "Simultaneous millimeter-wave multi-band channel sounding in an urban access scenario," in *Proc. of 9th European Conference on Antennas and Propagation (EuCAP)*, pp. 1–5, IEEE, 2015.

[21] V. Semkin, D. Solomitckii, R. Naderpour, S. Andreev, Y. Koucheryavy, and A. V. Räisänen, "Characterization of Radio Links at 60 GHz Using Simple Geometrical and Highly Accurate 3-D Models," *IEEE Transactions on Vehicular Technology*, vol. 66, no. 6, pp. 4647–4656, 2017.

[22] K. Tateishi, D. Kunta, and A. Harada, "Field experiments on 5G radio access using 15-GHz band in outdoor small cell environment," *Proc. of 26th Annual International Symposium on Personal, Indoor, and Mobile Radio Communications (PIMRC)*, Dec. 2015.

[23] T.-S. Yee, P.-S. Kooi, M.-S. Leong, and L.-W. Li, "Tropical raindrop size distribution for the prediction of rain attenuation of microwaves in the 10-40 GHz band," *IEEE Transactions on Antennas and Propagation*, vol. 49, no. 1, pp. 80–83, 2001.

[24] 3GPP, "Channel model for frequency spectrum above 6 GHz (Release 14)," 3GPP TR 38.900 V2.0.0, 2016.

[25] A. F. Molisch, *Wireless Communications*. John Wiley & Sons, 2 ed., 2011.

[26] R. Verdone and A. Zanella, *Pervasive Mobile and Ambient Wireless Communications: COST Action 2100*. Springer Science & Business Media, 2012.